Mon. Not. R. Astron. Soc. **000**, 1–11 (2002) Printed 12 January 2010 (MN LATEX style file v2.2)

When galaxies collide: understanding the broad absorption-line radio galaxy 4C +72.26

D.J.B. Smith[1,2⋆], C. Simpson[1], A.M. Swinbank[3], S. Rawlings[4] & M.J. Jarvis[5]
[1]*Astrophysics Research Institute, Liverpool John Moores University, Twelve Quays House, Egerton Wharf, Birkenhead, CH41 1LD, UK*
[2]*School of Physics and Astronomy, University of Nottingham, University Park, Nottingham, NG7 2RD, UK*
[3]*Institute for Computational Cosmology, Department of Physics, University of Durham, South Road, Durham DH1 3LE, UK*
[4]*Department of Astrophysics, University of Oxford, Denys Wilkinson Building, Keble Road, Oxford, OX1 3RH, UK*
[5]*Centre for Astrophysics, Science & Technology Research Institute, University of Hertfordshire, Hatfield, Herts, AL10 9AB, UK*

12 January 2010

ABSTRACT
We present a range of new observations of the 'broad absorption line radio galaxy' 4C +72.26 ($z \approx 3.5$), including sensitive rest-frame ultraviolet integral field spectroscopy using the Gemini/GMOS-N instrument and Subaru/CISCO K-band imaging and spectroscopy. We show that 4C +72.26 is a system of two vigorously star-forming galaxies superimposed along the line of sight separated by $\sim$1300$\pm$200 km s^{-1} in velocity, with each demonstrating spectroscopically resolved absorption lines. The most active star-forming galaxy also hosts the accreting supermassive black hole which powers the extended radio source. We conclude that the star formation is unlikely to have been induced by a shock caused by the passage of the radio jet, and instead propose that a collision is a more probable trigger for the star formation. Despite the massive starburst, the UV-mid-infrared spectral energy distribution suggests that the pre-existing stellar population comprises $\sim 10^{12}\,\mathrm{M}_{\odot}$ of stellar mass, with the current burst only contributing a further $\sim$2%, suggesting that 4C +72.26 has already assembled most of its final stellar mass.

Key words: galaxies: haloes – galaxies: high-redshift – galaxies: individual: 4C +72.26 – galaxies: starbusts – quasars: emission lines

1 INTRODUCTION

Powerful radio galaxies represent an important phase in the life of all massive galaxies. The tight locus they follow in the K-band Hubble diagram (Lilly & Longair 1982; Jarvis et al. 2001; Willott et al. 2003; Rocca-Volmerange et al. 2004) suggests that they are luminous ($\sim 3L^{*}$) galaxies whose stellar populations formed rapidly at very high redshift and have evolved passively since. Their descendants must inevitably be the most massive galaxies (with the most massive black holes) and, locally, such galaxies lie in the centres of galaxy clusters. During their most active formation phase, they are believed to regulate galaxy formation and growth by heating the intracluster medium with energy released from the continued accretion of material onto their central supermassive black holes (e.g. Best et al. 2006, Nesvadba et al., 2006, Nesvadba, 2009). However, most of the black hole growth must occur during a more luminous episode (or episodes) of activity when the black hole powers two oppositely-directed supersonic jets and has the characteristic Fanaroff & Riley (1974) Class II double-lobed morphology. Although the jets may be weak during most of the mass build-up (e.g. Martinez-Sansígre et al., 2005), powerful episodes of jet emission may cast their influence beyond the AGN's immediate environment (e.g. Rawlings & Jarvis, 2004). Understanding the relationship between the star-formation and accretion activity is essential to our understanding of massive galaxy evolution and requires observations of distant radio sources.

High-redshift radio galaxies (HzRGs) have generally been the most useful class of source, since their favourable orientation close to the plane of the sky means the host galaxy's stellar population is not swamped by the strong non-stellar continuum at ultraviolet and optical wavelengths, and ensures the overall spectral energy distribution is not affected by Doppler boosting of the synchrotron emission. Archibald et al. (2001, and also Reuland et al. 2003) found that the submillimetre luminosities of a sample of HzRGs were a strongly increasing function of redshift, which they claimed was due to increasingly youthful stellar populations (although this was subsequently cast in to doubt by Rawlings et al., 2004). The apparent lag between the assumed formation epoch ($z_{\mathrm{f}} = 5$) and the powerful AGN activity was explained by the time required for the central black hole to grow to $10^{9}\,\mathrm{M}_{\odot}$ (Archibald et al. 2002).

Deep spectroscopy of the $z = 3.8$ radio galaxy 4C 41.17 by Dey et al. (1997) revealed pronounced P Cygni-like features in the rest-frame ultraviolet which, coupled with the lack of polarization, implies that the UV light is dominated by a massive starburst with

⋆ E-mail: daniel.j.b.smith@gmail.com (DJBS)

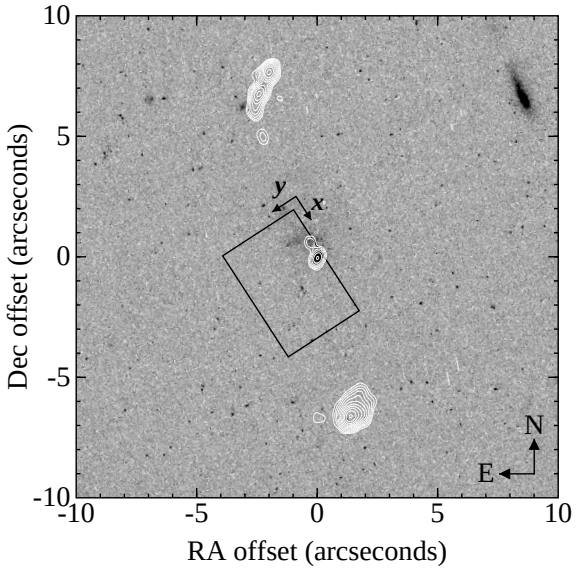

Figure 1. *Hubble Space Telescope* WFPC2 Planetary Camera image of 4C +72.26 in the F702W filter, overlaid with the region covered by the GMOS-N IFU observations. The reason for the misplacement of the IFU is given in the text. Some residual cosmic rays are still visible in the image. The white contours are from the 4.5 GHz radio map of Pentericci et al. (2000), kindly provided by C. De Breuck. The radio core has been aligned with the peak of the optical emission.

an age less than 16 Myr. Considering the close spatial correspondence between the radio, UV continuum, and Lyα emission, Bicknell et al. (2000) suggested that 4C 41.17 was undergoing a radio jet-induced starburst. While this scenario had been suggested before (Chambers et al. 1987; McCarthy et al. 1987; Rees 1989), 4C 41.17 provided the clearest observational example of the phenomenon. However, this picture is clearly at odds with that proposed by Archibald et al. (2002).

In this paper we discuss our observations of the $z \approx 3.5$ source 4C +72.26, also known as 6C 1909+72, or TX J1908+7220. Although originially classified as a 'broad absorption line radio galaxy' from its optical spectrum spectrum (Dey 1999; de Breuck et al. 2001), we demonstrate that the absorption features are P Cygni profiles characteristic of a massive starburst which provides the entire rest-frame ultraviolet continuum.

The format of this paper is as follows. In Section 2 we describe the new observations of 4C +72.26, and in Section 3 we present and discuss our major results, including the evidence for two star-forming systems superimposed along the line of sight. In Section 4 we present a new analysis of the spectral energy distribution of 4C +72.26, and in Section 5 we discuss our interpretation for the source. Finally, we summarize our conclusions in Section 6. Throughout this paper we adopt a cosmology with $H_0 = 72\,\mathrm{km\,s^{-1}\,Mpc^{-1}}$, and $\Omega_\mathrm{m} = 1 - \Omega_\Lambda = 0.26$ (Dunkley et al. 2009).

2 OBSERVATIONS

2.1 Imaging

Images of 4C +72.26 were taken through the K' filter with the Cooled Infrared Camera and Spectrograph for OHS (CISCO; Motohara et al. 2002) on Subaru Telescope on the night of UT 2000 July 13. A total of 64 separate 20-second exposures were taken, with 8 cycles of an 8-point dither pattern. Due to CISCO's reset anomaly, the first exposure in each cycle was discarded, giving a total exposure time of 1120 s. These images were dark-subtracted, normalized, and median-filtered to provide a flatfield which was applied to each individual exposure. These were then coadded using offsets calculated from the centroids of objects detected in each frame. There was thin cloud at the time of the observations so photometric calibration was performed relative to three stars in the field which are present in the Two Micron All Sky Survey (2MASS) catalogue. No colour corrections were applied to transform from the CISCO K' filter to the 2MASS K_s filter since they have very similar transmission profiles. The 5-σ magnitude limit of these data is $K_s = 20.8$, measured in a $2''$ aperture.

We have also obtained an archival HST image of 4C +72.26, taken using the Wide-Field and Planetary Camera 2 with the F702W filter for two 3000-second integrations (PI G. Miley). The two frames were combined with cosmic-ray rejection using the IRAF/STSDAS task `crrej` and the absolute flux scale was determined from keywords in the image header. These data are presented in figure 1.

2.2 Longslit spectroscopy

A K-band spectrum of 4C +72.26 was taken with CISCO on UT 2000 July 14. A 1-arcsec slit was used at a position angle of 33° to align the slit with the extended radio structure (Pentericci et al. 2000). This setup provided a resolution $\lambda/\Delta\lambda \approx 300$ at a dispersion of $\sim 8.6\,$Å pixel^{-1}. The source was acquired by blind offsetting from a nearby USNO star; the offsets of $38.6''$ East and $6.4''$ North had been measured from the K-band image taken the previous night. Twenty exposures of 200 s each were taken, with the target alternating between two positions along the slit separated by 10 arcsec. One image in each pair was subtracted from the other to provide first-order sky removal. Pixel-to-pixel sensitivity variations were removed by dividing by the normalized K' flatfield used in the reduction of the imaging data. Curvature in the sky lines was corrected by cross-correlating each row (spatial element) of the longslit spectrum against the central row and shifting it by the resulting amount. Residual sky emission was then removed by fitting a second-order polynomial at each wavelength position. Wavelength calibration was performed by fitting a second-order polynomial to identified sky lines, with an rms of 16 Å.

A spectrum of the nearby F8 star SAO 9358 was taken and modelled as a 6140 K blackbody to determine the relative sensitivty as a function of wavelength, and the absolute flux scale derived from a spectroscopic observation of the UKIRT Faint Standard FS 147 (Hawarden et al. 2001). From cuts in the spatial direction of these spectra, the seeing at the time of the observations was estimated to be 0.5 arcsec.

2.3 GMOS-N Integral Field Spectroscopy

4C +72.26 was observed using the GMOS-N instrument in IFU mode, between 30 May and 27 August 2006 under program ID GN-2006A-Q-36. The instrument was used in single slit mode, providing a field of view of $5''\times3.5''$ at a position angle 33° East of North, with the R400 grating set to a central wavelength of 8037 Å. Again, blind offsetting was required, and the Phase 2 document for the observations provided the accurate relative offset from the USNO star to the target, but included only nominal catalogue positions for the

offset star and target. However, the blind offsetting was performed by resetting the telescope pointing after peaking up on the offset star, and then moving to the *absolute* astrometric coordinates of the target. Since the USNO and 6C catalogues have different absolute astrometric calibrations, this introduced a positional offset error of $1.6''$ which resulted in the core of the target lying close to the edge of the instrument's field of view (Fig. 1).

Ten 3600-second exposures were taken, and the data were reduced using standard IRAF packages as well as making use of custom `IDL` routines specifically designed for the GMOS-N IFU (Swinbank et al. 2003, 2006). The data were de-biased, flat-fielded, corrected for the pixel-to-pixel CCD response, and wavelength calibrated based on arc lamp exposures taken with the same instrumental setup at the same time as the science observations. The sky lines were subtracted making use of the sky fibers interspersed with the science fibers on the combined CCD frames, and cosmic rays were rejected from the individual frames, with additional flattening of each exposure making use of empty regions of spectra to remove any remaining gradients in the frames. The individual exposures were then mapped into a separate data cube for each 3600s integration. The cubes were then combined to the nearest "spaxel" making use of a 3σ clipping algorithm, with offsets based on a 2D fit to the continuum emission profile in each data cube. The data were flux calibrated based on observations of the spectrophotometric standard star Wolf 1346 using the same setup as for the science observations, and the generated flux solution was applied to the stacked cube.

3 RESULTS

We present optical spectra of 4C +72.26 in Figs. 2; whilst the upper spectrum appears very similar to the long slit spectrum presented in De Breuck et al (2001), our IFU data also have wavelength coverage up to ~ 8400Å. In addition to the narrow emission lines of Lyα and He II, several deep broad absorption troughs can be seen. These are the features which led Dey (1999) to refer to 4C +72.26 as a 'broad absorption line radio galaxy'.

In Fig. 3 we show two narrow-band images from our stacked datacube. In the upper panel the Lyα emission is shown, whilst the lower panel shows the spatial distribution of the continuum between 7067 Å and 7211 Å (this region was chosen since it is free of both absorption and emission line features). Although the target is not centred in our field of view, we can see that the Lyα emission has a greater extent than the continuum emission. The different properties of these two regions are shown more clearly in Fig. 2, which shows spectra extracted around the continuum peak (pixel 10,1)[1] and the Lyα emission peak (pixel 4,1). Comparing to Fig., 1, we infer that the compact southern knot (which is unresolved in the Planetary Camera image, implying a size < 500 pc) is the site of most of the continuum emission, while the diffuse emission seen to the north and northeast has a significant contribution from the C IV and He II emission lines. At the very edge of our datacube, these lines are still visible but we do not detect any continuum emission.

3.1 The emission lines

To better constrain the emission line characteristics of 4C +72.26, we extracted several wavelength regions of particular interest from

[1] We denote the bottom-left pixel of Fig. 3 as (0,0).

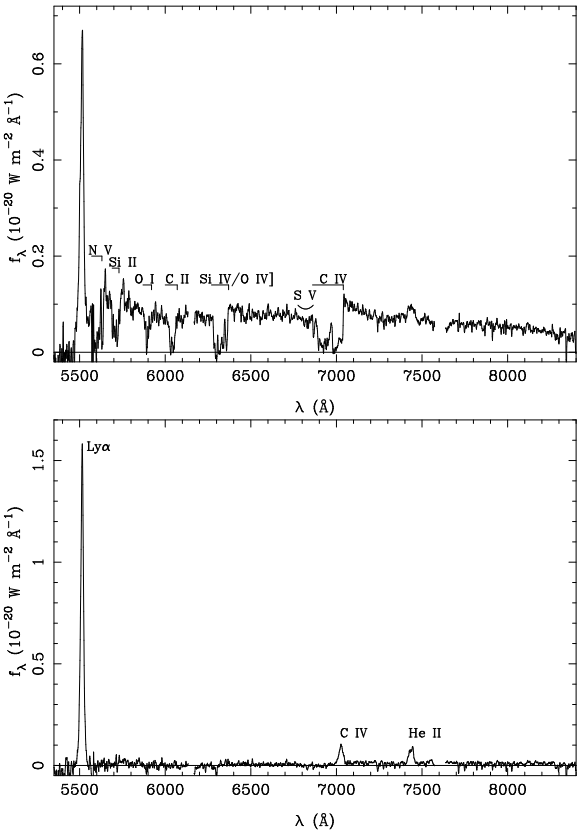

Figure 2. GMOS-IFU spectra of 4C +72.26 extracted from 3×3-pixel regions around the continuum peak (top) and Lyα emission peak (bottom). Both spectra have been smoothed with a 3-pixel boxcar filter. The locations of emission lines are shown in the bottom panel, while the absorption features are labelled in the top panel. The two small gaps in the spectral coverage centred on $\sim$6150 and $\sim$7600Å are due to the chip gaps on the GMOS CCDs.

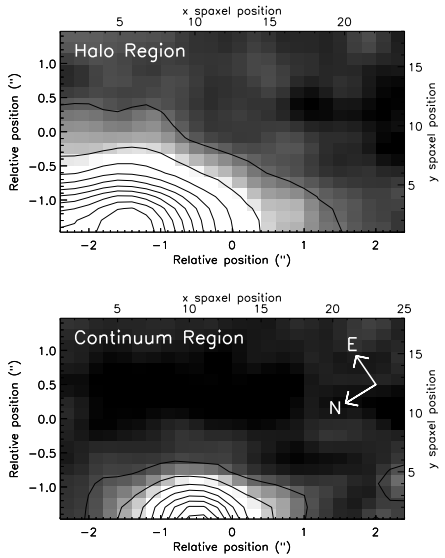

Figure 3. Lyman-α narrow-band (top) and continuum (bottom) images from the data cube. It is clear that the extensive Lyman-α halo is offset from the peak intensity of the continuum emission. The observations were taken at a position angle of 33° East of North using the GMOS-N instrument in single-slit IFU mode.

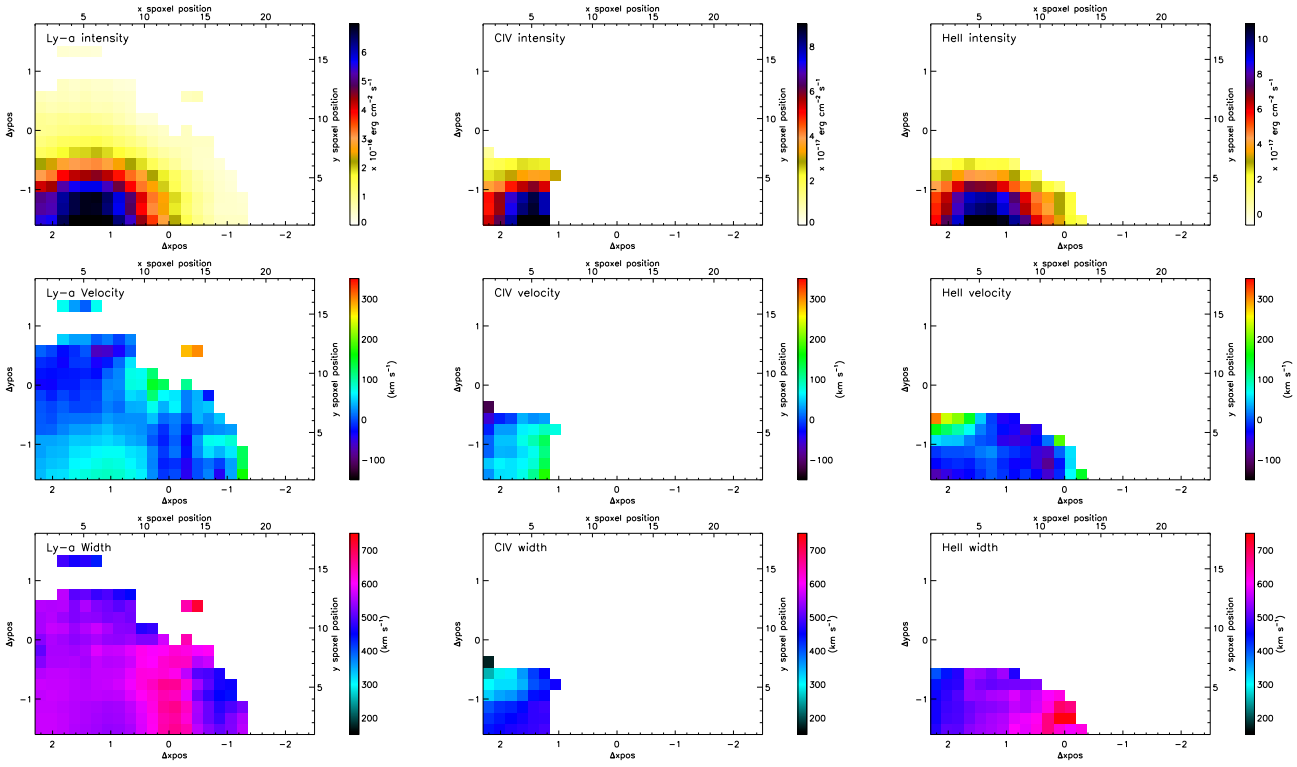

Figure 4. Lyman-α_{1216}, and C IV$_{1549}$, He II$_{1640}$ emission line intensity, velocity and linewidth as a function of position within the data cube. All values are given in the rest-frame of 4C +72.26, and each colour bar has the same velocity scale. Some of the structure in the width of the Lyman-α emission lines is due to the fact that the Lyman-α emission has two separate components (see section 3.1). The poor positioning of the object within the IFU field-of-view is due to an error in the execution of the observation request. The orientation in each of the figures is the same as in figure 3.

the datacube, corresponding to the regions exhibiting redshifted Lyα_{1216}, C IV$_{1549}$, and He II$_{1640}$ emission. The emission lines in each wavelength region of interest were fit with a one-dimensional Gaussian profile, using a χ^2 minimisation procedure which allowed the central wavelength, linewidth and normalisation to vary. The spectra were weighted using a 2D gaussian profile of 5×5 pixels centred around each spaxel to account for the atmospheric seeing ($\sim$0.6″$\approx$3 spaxels) in these data, and smoothed by 3 pixels ($\sim$ 4.1Å) in the wavelength direction. To determine whether an emission line was present in a given spaxel, we calculated values of χ^2 for both a flat continuum, and a single Gaussian emission line profile. We required a minimum $\delta\chi^2$ of 25 (S/N of 5) to detect an emission line. In this way, all of the non-blank emission line spaxels in figure 4 are detected at $> 5\sigma$. The results of the fitting procedure (intensity, central wavelength offset and velocity width) are shown in Fig. 4.

It is apparent that the emission lines have their maximum intensity away from the continuum peak. The C IV line is, in fact, undetectable at the continuum peak due to the deep absorption trough. We place limits of 360±210 km/s, on any possible velocity shear of the Lyman-α emission line over $\sim$25 kpc in projection. Lyα (where the signal-to-noise ratio is the highest) shows only a small region, roughly a square arcsecond in size, where the gas is redshifted by about 100 km s^{-1}, approximately 0.8″ to the North-East of the continuum peak; this feature is not seen in He II, despite both lines showing the same increase in velocity dispersion close to the continuum peak.

Unlike the profiles of the HeII and CIV emission lines, which are consistent with a single gaussian component at $z = 3.534$, it is clear that the Lyα emission line profiles measured in our data cubes consist of two components. To investigate this further, we fit the Lyα emission in 4C +72.26 with two Gaussian profiles and the results are shown in Fig. 5. The model is a good approximation to the observed profiles and, although the relative strengths of the two components vary between spaxels, their redshifts are virtually constant, at $z = 3.5334 \pm 0.0008$ and $z = 3.5363 \pm 0.0005$ for the two components. Their velocity dispersions are also almost constant, with the Gaussians having FWHMs of 11.5 $\pm$ 0.5 Å (625 $\pm$ 30 km s^{-1}) and 4.8 $\pm$ 0.2 Å (260 $\pm$ 10 km s^{-1}), respectively. This decomposition also trivially explains the structure seen in Fig. 4. The increased redshift to the NE of the continuum peak is due to an increased contribution from the redder velocity component, while the increased velocity dispersion is due to the bluer component (which dominates the total flux, and is also broader) being broadest at this location.

3.2 The Absorption Lines

Although the spectrum of 4C +72.26 displays very broad absorption features similar to those of a broad absorption line quasar (BALQSO), with the C IV trough extending blueward to $\sim$ 7000 km s^{-1}, more species are seen in absorption in 4C +72.26 than in BALQSOs. In addition to the C IV and Si IV troughs, sharper absorption features are seen just shortward of the predicted wavelengths of O I$_{1302}$ and C II$_{1335}$. Such features were also seen in 4C 41.17 (Dey et al. 1997) and nearby star-forming galaxies such as NGC 1741 (Conti, Leitherer & Vacca 1996).

To better understand the relationship between the star-forming

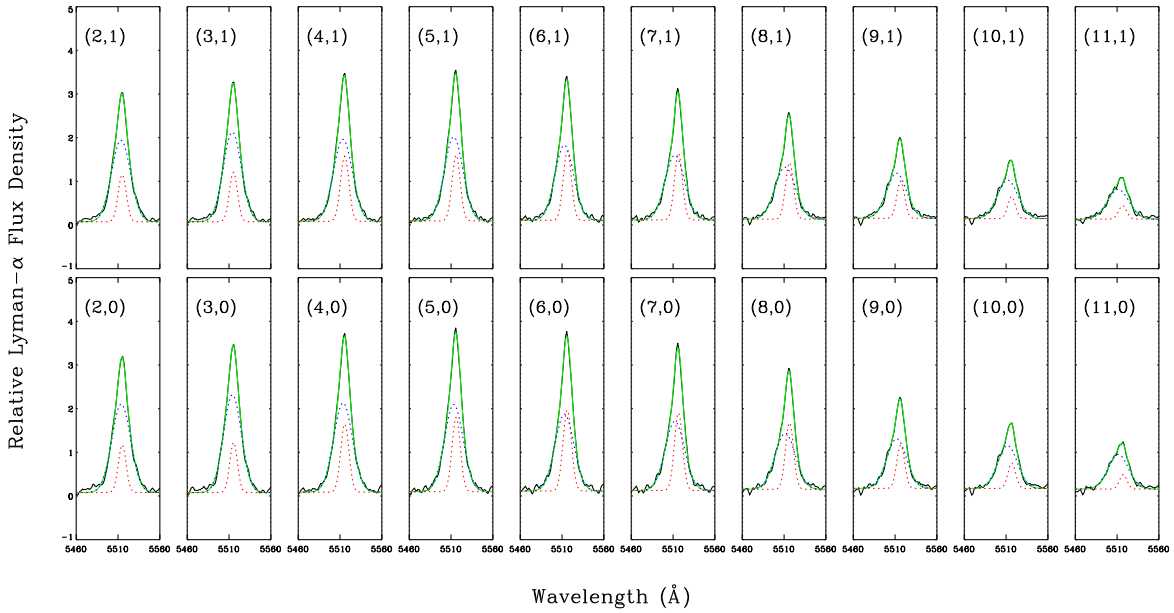

Figure 5. The results of fitting our double-Gaussian model to the Lyman-α emission in 4C +72.26. The data are shown as the black solid line with the spaxel indices displayed in the top left corner of each plot, whilst the best fit model (green dotted line) is a linear summation of the blue and red dotted components, whose central wavelengths and widths are shown in angstrom on the left and right sides of each plot, respectively. The two best-fit models vary remarkably little over the nuclear region of 4C +72.26. Spaxel numbers count from (0,0) at the bottom left of the IFU as shown in Fig. 4, with the peak of the continuum being at (10,0).

region(s) and the AGN, we attempted to derive a redshift for the starburst by Fourier cross-correlating a spectrum extracted from the core of 4C +72.26 with that of NGC 1741 (Conti et al. 1996). Fourier cross-correlation exploits the easily-derived fact that the Fourier transform of the sum of two functions (here, spectra) is equal to the sum of the transforms of the two functions. For this analysis, only the region between the Lyα and He II lines was used, to avoid problems with the strong emission lines (C IV is not observed at the continuum peak of the source; Fig. 4). The IRAF task `fxcor` was used to perform the cross-correlation, returning the amplitude of the correlation function at a range of discrete velocities.

The cross-correlation function suggests the presence of two absorption systems, separated by 1300 ± 200 km s^{-1} along the line of sight. The results of this modelling are shown in Fig. 6. The velocities of the two components, corresponding to redshifts of 3.5203 ± 0.0011 and 3.5401 ± 0.0027 (where the errors are derived based on the standard deviation of the individual spaxel redshifts), suggesting that the continuum emission observed in 4C +72.26 is the result of two interacting starburst galaxies, moving relative to one another with a line-of-sight velocity of $\sim 1300\,\mathrm{km\,s^{-1}}$.

To confirm this interpretation, we have constructed a spectrum of two star-forming regions using NGC 1741 as a template. We fit a smooth continuum to the unabsorbed regions of the NGC 1741 and derive the optical depth as a function of wavelength, $\tau(\lambda)$. A spectrum can then be constructed as

$$I(\lambda) = e^{-\tau(\lambda/(1+z_1))}(1 + fe^{-\tau(\lambda/(1+z_2))})$$

where z_1 and z_2 are the redshifts of the star-forming regions, and f is the relative luminosity of the background system, compared to the foreground one. This assumes that the foreground system completely covers the background one, which appears to be the case since the observed flux drops to zero in the C IV absorption trough.

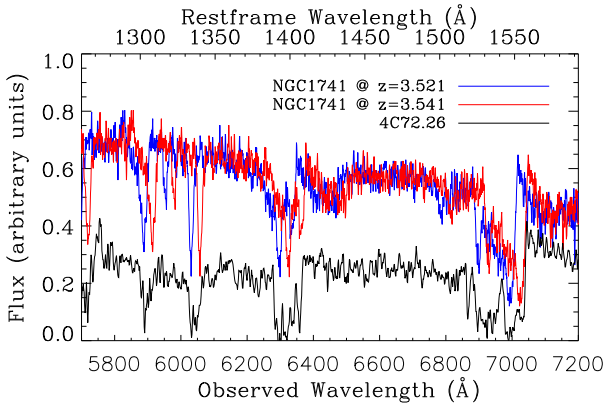

Figure 7. A comparison between the observed spectrum at the core of 4C +72.26 and the spectrum of NGC 1741 at two separate redshifts corresponding to the best-fit redshifts from our Fourier cross-correlation (blue and red, corresponding to the lower- and higher-redshift systems, respectively). Note how two absorption systems are able to reproduce the structure in the C II and C IV troughs shown in the spectrum of 4C +72.26 (shown in black).

To achieve this, we had to increase the optical depth in the two systems, compared to that derived from the NGC 1741 spectrum. And, as shown in Fig. 7, this deep trough is seen at a wavelength consistent with the lower-redshift ($z = 3.520$) system, indicating that it must lie in front of the higher-redshift ($z = 3.540$) one. The depth of the C IV trough produced by the background (redder) system sets $f \approx 5$, since the continuum here is due to the foreground system only.

We can also use the rest-frame ultra-violet continuum luminosity to estimate the star formation rate associated with 4C +72.26

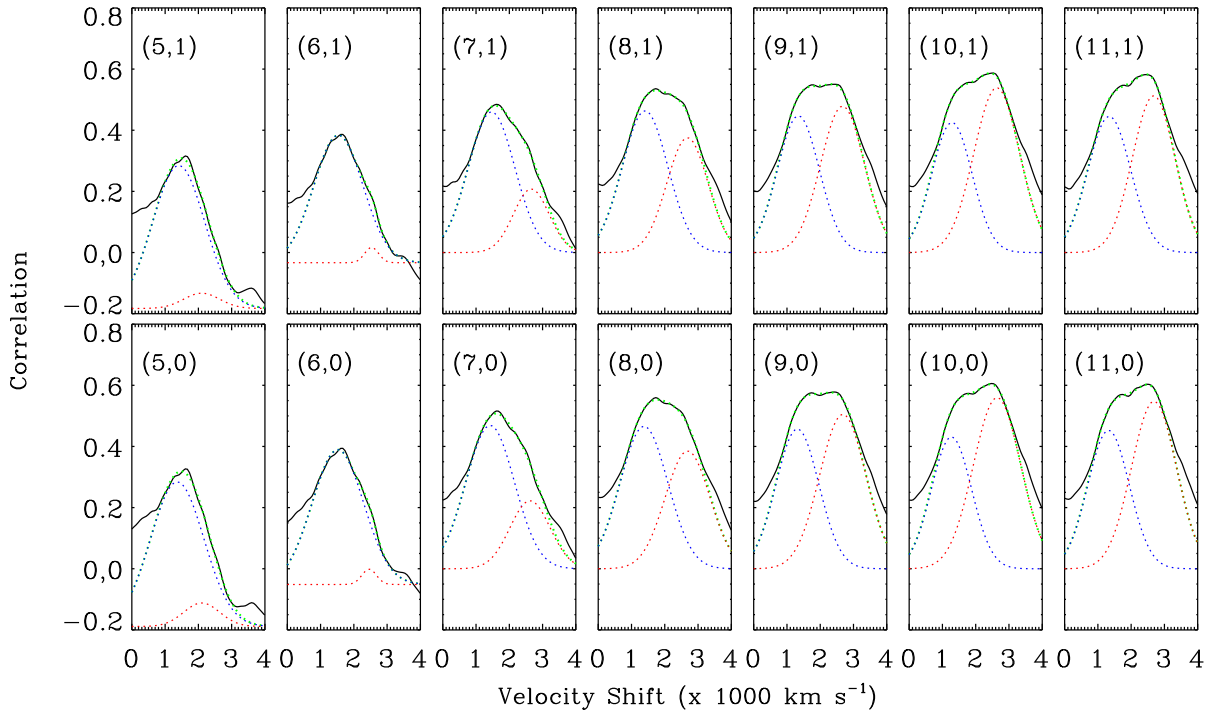

Figure 6. The results of our Fourier cross-correlation between the core spaxels of 4C +72.26 (with the positions shown by the pixel co-ordinates in the top left of each frame), and the template spectrum of typical starburst galaxy NGC1741 (redshifted to $z = 3.5$ before cross-correlating). The peaks in the correlation function (black solid line) have been approximated by a best-fit model (green dotted lines), which is the sum of a a flat continuum and two Gaussian components (blue and red dotted lines).

using the calibration of Madau, Pozzetti & Dickinson (1998). Since we have clearly missed some of the continuum in our IFU observations, we have rescaled the spectrum to make its flux scale consistent with the *HST* F702W measurement of 8.18 μJy (in a 4-arcsecond aperture). A factor of 1.75 upward correction is required, which is reasonable since the compact core lies very close to the edge of the IFU's field of view (Fig. 1) and therefore seeing will redistribute almost half the flux outside our datacube. We derive a luminosity density at 1500 Å of $3.1 \pm 0.5 \times 10^{35}$ W Å^{-1} and hence a star-formation rate of 300 $\mathrm{M}_{\odot}$ yr^{-1} (Salpeter IMF) or 680 $\mathrm{M}_{\odot}$ yr^{-1} (Scalo IMF), with a $\sim$16% uncertainty associated with each value. Although these numbers differ by a factor of two, they are both an order of magnitude lower than that derived from the far-infrared luminosity (4000 ± 700 $\mathrm{M}_{\odot}$ yr^{-1}) or PAH emission (~ 8000 $\mathrm{M}_{\odot}$ yr^{-1}; Seymour et al. 2008).

We can also derive the SFR based on the starburst models of Leitherer et al. (1995), in a manner similar to that demonstrated in Dey et al. (1997) for 4C 41.17. As with 4C 41.17, we find evidence for S V$_{1502}$ absorption, although the presence of two superposed absorption systems results in a large width of the feature ($\sim 80 \pm 40$Å). This, coupled with its low equivalent width, may explain why it is not apparent in the Keck spectrum of De Breuck et al. (2001), which was extracted over a larger spatial region. As this feature is only seen in O stars (Walborn, Nichols-Bohlin & Panek 1985; Walborn, Parker & Nichols 1995), it implies a young stellar population. However, a single power-law fit to the continuum of the top panel of Fig. 2 over the range 5800–8000 Å gives $F_{\lambda} \propto \lambda^{-0.51 \pm 0.05}$, implying either substantial reddening or an additional red spectral component; we return to this point in Section 4. The Leitherer et al. models suggest that a continuously star-forming population with a rate of 1 $\mathrm{M}_{\odot}$ yr^{-1} has a luminosity at 1500 Å of between $\log(L_{1500}/\mathrm{W\,A}^{-1}) = 32.25 - 33.16$ for ages of 1–9 Myr. which corresponds to a star formation in the range 210–1700 $\mathrm{M}_{\odot}$ yr^{-1}. Despite a broad range of estimates of the star-formation rate in 4C +72.26, it is clear that a massive starburst is underway with a rate of $\sim$1000 $\mathrm{M}_{\odot}$ yr^{-1}, comparable with the most extreme rates seen in the Universe (e.g. in SCUBA galaxies, Smail, Ivison & Blain, 1997, or Ivison et al., 2007). In both cases, approximately 80% of the total star formation occurs in the background galaxy.

3.3 K-band spectroscopy of 4C +72.26

Fig. 8 shows our CISCO K-band spectroscopy of 4C +72.26. In order to study the emission lines in 4C +72.26, we approximated the spectrum using a simple model consisting of four Gaussian components and a continuum component that is flat in F_{λ}. In fitting the spectrum with this simple model, we required the redshifts of the narrow Hβ and [O III] components to be equal since they arise from the same emission-line gas, whilst the broad component's central wavelength was allowed to vary. The widths of the two [O III] lines were set to be equal, and their flux ratio constrained to be 3. The best fit model is shown in Fig. 8; we find that our simple model adequately describes our data; the broad component of the Hβ emission has a best-fit redshift of $z = 3.5407 \pm 0.0066$, while the narrow emission lines are blueshifted by $\sim 460\,\mathrm{km\,s}^{-1}$, although this is approximately equal to the 1σ error on the redshift of the broad Hβ component, so the two redshifts are formally consistent.

With the results of our model fitting, we can use the calibration

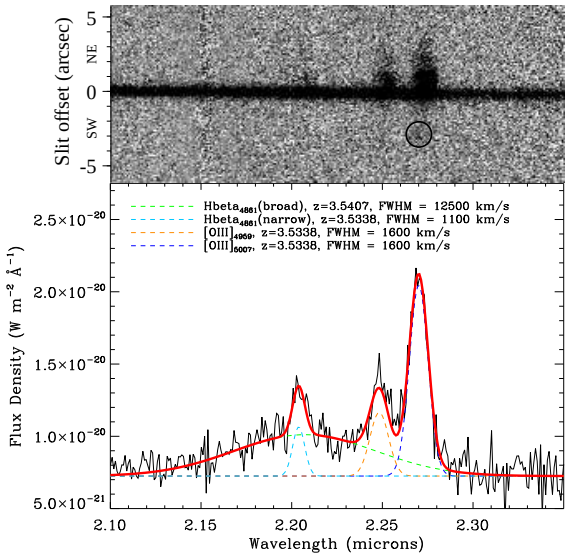

Figure 8. CISCO K-band spectroscopy of 4C +72.26, showing spatially-extended narrow emission lines of Hβ, and [O III]. Top: two-dimensional spectrum, with [O III] emission visible on both sides of the unresolved continuum. The K-band continuum peak is coincident with the optical peak, and therefore the assumed position of the radio core. The circle indicates the location of the [O III] line emission discussed in the text. Bottom: one-dimensional spectrum, extracted through a 1-arcsecond aperture, with five-component fit overlaid. The five components are flat continuum level of 7.2×10^{-21}W m^{-2} Å^{-1}, broad Hβ (green, dashed line), narrow Hβ (light blue dotted-dashed), [OIII]$_{4959}$ (orange dot-dashed), and [OIII]$_{5007}$ (dark blue dotted).

from McLure & Jarvis (2002) to determine the mass of the central black hole from the FWHM of the Hβ emission line:

$$\frac{M_{\rm bh}}{\rm M_\odot} = 4.74 \left(\frac{\lambda L_{5100}}{10^{37}\rm W}\right)^{0.61} \left[\frac{\rm FWHM(H\beta)}{\rm km\ s^{-1}}\right]^2. \qquad (1)$$

The derived value of $(1.8 \pm 0.2) \times 10^{10}\,\rm M_\odot$ (the error quoted is from the fit) is larger than the most massive black holes in the McLure & Jarvis (2004) sample, although the 1σ uncertainty in the calibration is a factor of 2.7. However given that 4C +72.26 was originally discovered through low-frequency radio emission we might expect that it is aligned closer to the plane of the sky than the majority of optically selected quasars. If the broad-line region is akin to a rotating disk then we would expect, on average, broader emission lines (see e.g. Jarvis & McLure, 2006). Therefore, although our black-hole mass estimate is subject to uncertainties of order a factor of 5, we can say with certainty that we are observing an extremely massive black hole.

We note that the line-emitting gas is only present on the North-East side of 4C +72.26. We associate this with the foreground since there is a tentative one-sided jet at radio wavelengths and this is the longer radio arm, suggesting a shorter light travel-time to the observer, although doubt remains as to whether this is in fact the case. McCarthy, van Breugel & Kapahi (1991) suggested that emission-line asymmetries were due primarily to differences in the density on the two sides of the nucleus, supporting this with evidence of a correlation between the side with the strongest line emission and the side with the shortest radio arm. However, this is not the case for 4C +72.26 where the approaching arm is the longer of the two, and so we instead suggest that there is an extensive dust disc obscuring the far side of the emission-line region. The near-side line emission extends for $\sim 2.5''$ (18 kpc) from the nucleus, and close inspection of the longslit spectrum reveals faint line emission located ~ 2.5" from the nucleus on the far side of the source, which we speculate is material just beyond the extent of this putative disc (figure 8). We also examined an archival WHT-ISIS spectrum of 4C +72.26, which shows the Lyman-α emission extending for $\sim 8''$ in the NE direction, without any emission being detected on the SW side of the core; this is not surprising given the ease with which Lyman-α photons may be absorbed. Comparing the surface brightness of the [O III] emission on both sides of the nucleus, we conservatively estimate an asymmetry of > 7 (3σ), implying $A_V > 1.9$ (adopting the SMC extinction law of Pei 1992). Assuming the relationship between gas column density and extinction derived by Bohlin, Savage & Drake (1978), we calculate $N_{\rm H} > 3.5 \times 10^{21}\,\rm cm^{-2}$. If this column persists across an entire 18-kpc-radius disc, then the total mass of gas contained within it is $M_{\rm gas} > 3 \times 10^{10}\,\rm M_\odot$, which would be sufficient to power the starburst at its present rate for at least a few million years. This estimate is consistent with the value of $4.5 \times 10^{10}\,\rm M_\odot$ of $\rm H_2$ conservatively estimated by Papadopoulos et al. (2000) from their CO(4–3) observations. Our proposed extent for the disc is marginally consistent with the upper limit of $4''$ for the extent of the CO, for which Papadopoulos et al. derive a dynamical mass of $6 \times 10^{11} (\sin i)^{-2}\,\rm M_\odot$.

We can also use the ratio of the fluxes in the broad and narrow components of the Hβ line to estimate the attentuation to the broad line region within 4C +72.26. If we assume an intrinsic ratio of broad to narrow Hβ of 40 (e.g. Jackson & Eracleous 1995), then the ratio determined from our four-component Gaussian fit corresponds to a factor of 4.1 in extinction at 4861 Å, equivalent to $A_V \approx 1.4$, although this is highly uncertain given the available data.

4 SPECTRAL ENERGY DISTRIBUTION OF 4C +72.26

We have compiled archive photometry of 4C +72.26, similar to the results of Seymour et al. (2008), in Table 1. However our new observations demonstrate that the continuum is dominated by a QSO at near-infrared wavelengths, and a luminous starburst in the optical/UV, which were not included in the Seymour et al. SED analysis.

The luminosity of the QSO component is well constrained by the 10–20-μm photometry (observed frame), since this wavelength range is redward of the peak of stellar emission, and blueward of the thermal emission from the starburst-heated dust. Demanding that the model QSO component (a median radio-loud QSO model from Elvis et al., 1994) alone fits the photometry in this region also provides strong constraints on the amount by which it can be extinguished. The F702W photometry requires $A_V > 0.7$ or else the QSO emission alone will exceed the total flux. The rest-frame equivalent width of the broad Hβ line is 86 Å, and for this to be consistent (at the 2σ level) with the distribution of local, bright QSOs from Miller et al. (1992) requires that at least 41 per cent of the K-band continuum light is from the QSO, and this in turn demands $A_V < 1.2$. This relatively narrow window of acceptable extinction values is even smaller if an LMC or Milky Way extinction law is used, since they are shallower in the ultraviolet and hence a larger visual extinction is needed to produce the required UV attenuation.

With these constraints, the reddened QSO still contributes to the rest-frame ultraviolet emission, and explains why the spectrum is much redder than would be expected for a young stellar popula-

Table 1. Photometry of 4C +72.26 used in our SED fitting analysis (Fig. 9). These data are compiled from several different publications as shown in the table. The errors are quoted to 1σ; where limits are given, they correspond to 3σ.

Photometric Band	Flux Density (μJy)	Instrument	Reference
F702W	8.18 ± 0.16	WFPC2	This work
$K_{\rm s}$	134 ± 7	CISCO	This work
$K_{\rm s}$ (line-corrected)	109 ± 11	CISCO	This work
3.6μm	200 ± 20	IRAC	Seymour et al., 2007
4.5μm	229 ± 23	IRAC	
5.8μm	241 ± 25	IRAC	
8.0μm	480 ± 48	IRAC	
12μm	840 ± 100	ISOCAM	Siebenmorgen et al., 2004
16μm	1320 ± 70	IRS	Seymour et al., 2008
24μm	1910 ± 100	MIPS	Seymour et al., 2007
70μm	16200 ± 1900	MIPS	
160μm	<63300	MIPS	
350μm	90000 ± 15000	SHARC-II	Greve et al., 2006
450μm	33000 ± 17000	SCUBA	Reuland et al., 2004
850μm	13500 ± 1300	SCUBA	Papadopoulos et al., 2000
1250μm	<3000	PdBI	

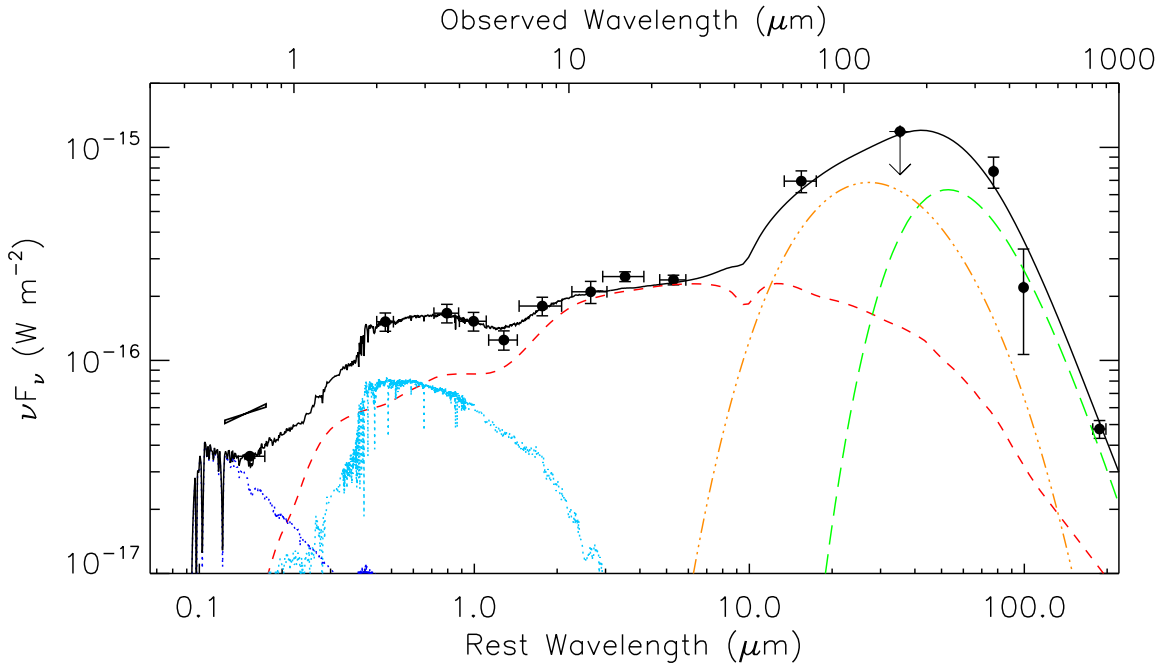

Figure 9. Spectral energy distribution of 4C +72.26; the best fit model (solid line) is the sum of five components: a 30-Myr old starburst population (blue dotted line), a 1-Gyr stellar population (light blue dotted line), a radio-loud QSO template (red dashed), a warm dust component (orange dot-dashed) and a modified grey-body cold dust profile (green dashed) taken from Seymour et al. (2008). The bow-tie above the spectrum in the rest-frame ultraviolet indicates the slope of the continuum as measured from the spectrum. For details of the fitting and the photometry see section 4 and table 1.

tion (Section 3.2). Dey et al. (1999) noted that the ultraviolet continuum emission in 4C +72.26 was unpolarised, consistent with our SED analysis in excluding a dominating scattered QSO component at these wavelengths. In fact, the young stellar population (which we model with a 30-Myr-old simple stellar population from the BC03 models of Bruzual & Charlot 2003) must be unreddened for the overall spectral shape to remain consistent with our GMOS observations. The luminosity of the young stellar component is therefore tightly constrained by the F702W photometry.

As the QSO must contribute between 40–70 per cent of the K-band continuum light, and the young stellar population only contributes $\sim$ 10 per cent, there must be a further component which provides 20–50 per cent of the continuum light. Since this component must peak at $\lambda_{\rm rest} \sim 1\,\mu$m, we assume it is stellar in origin, and a natural interpretation is a more evolved population of stars.

However, we note that this component alone must have $17.7 < K < 18.7$, which places it between 1.1 and 2.1 magnitudes brighter than the polynomial fit to the K–z relation of Willott et al. (2003). However, we note that this is consistent with the distribution of $K-$band magnitudes at $z > 1.8$ in Jarvis et al. (2001, and more recently those in Bryant et al., 2009) where there appears to be a slight turnover in the K–z relation. Furthermore, the

typical scatter of 0.6 magnitudes across the whole of the K–z diagram and the correlation between host galaxy mass and radio luminosity previously discussed means that it is not unreasonable to observe such a magnitude for this particularly powerful high-redshift radio source. As the K–z relation closely follows the passive evolution of a present-day $3L^*$ galaxy that formed at a redshift $z_\mathrm{f} = 10$, this stellar component would evolve into a very luminous (8–20L^*) galaxy by the present epoch, unless it formed more recently. We, somewhat arbitrarily, use an unreddened 1-Gyr-old population, whose age corresponds to $z_\mathrm{f} = 6.7$. The mass of these stars required to fit the SED is $1.8 \times 10^{12}\,\mathrm{M}_\odot$ (assuming a Initial Mass Function from Chabrier, 2003, and Solar metallicity), although this is not very sensitive to the assumed age, since younger populations, although they possess an intrinsically smaller mass-to-light ratio, must be reddened in order to maintain the overall shape of the SED. Unfortunately, we lack the detailed spectral coverage in the 1–2 μm range to remove the degeneracy between age and extinction for this population, and we can obtain acceptable fits with a range of values, although all require a mass of $> 1 \times 10^{12}\,\mathrm{M}_\odot$. Populations with exponentially-declining star formation rates can also fit this population, provided the e-folding time is less than the age and they are reddened; an additional unreddened young population is also required, however.

In summary, our best-fit spectral energy distribution consists of five components:

- a 30-Myr-old simple stellar population from Bruzual & Charlot (2003), with a mass of $2 \times 10^{10}\,\mathrm{M}_\odot$,
- a 1-Gyr simple stellar population, also from Bruzual & Charlot (2003), with a mass of $1.8 \times 10^{12}\,\mathrm{M}_\odot$,
- a median radio-loud QSO template from Elvis et al. (1994) which suffers 1.2 magnitudes of extinction, according to the Small Magellanic Cloud law of Pei et al. (1992)
- a warm dust component described by a power-law with an index of two and exponential cutoffs at high and low frequency,
- a modified black body with a temperature of 50K and emissivity index $\beta = 1.5$ (following the results of Seymour et al. 2008).

It is clear from Fig. 9 that the overall SED is readily split into the ultraviolet/optical/near-infrared regime (fit by the first three components listed above), and the far-infrared region (fit by the last two components), with effectively no cross-talk between these two regimes. Our fit to the far-infrared region is very similar to that of Seymour et al. (2008), while our fit over the two decades in wavelength from 0.1–10 μm is constrained by nine photometric measurements, plus information from our spectroscopy.

We note that our fit significantly underestimates the 16-μm flux measured by *Spitzer*, but the IRS spectrum of 4C +72.26 clearly shows strong PAH emission which is not included in the QSO SED (Seymour et al. 2008). The need to include warm dust emission in addition to the QSO SED (whose far-infrared continuum is also produced by thermal dust emission) indicates a substantial extra heating source, consistent with the massive starburst observed in our GMOS spectrum. Finally, we note the good agreement between our estimates of the foreground extinction to the QSO derived from the Hβ emission ($A_V = 1.4$) and the SED ($A_V = 1.2$).

5 DISCUSSION

A comparison of the results of our Lyα fitting and our Fourier cross-correlation of the continuum properties of 4C +72.26 are shown in Fig. 10. The redshift of the broad Hβ component is consistent with the redshift of the redder (background) starburst, at $z = 3.5407 \pm 0.0066$, and we identify this as the redshift of the radio-loud AGN. Although both Lyα emission-line systems are formally consistent with this redshift (due to the large uncertainties associated with the continuum and broad-line redshifts), we identify them as the approaching sides of two bidirectional outflows, with the receding sides hidden by the large-scale dust disc described in Section 3.3. This asymmetric obscuration can also explain the lack of spatial coincidence between the peaks of the Lyα and continuum emission.

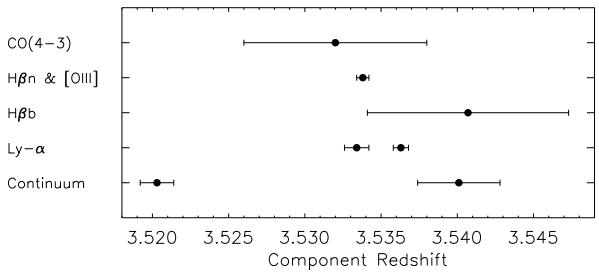

Figure 10. A comparison between the redshifts derived for each of the different observables. The Lyman-α redshifts and those of the Fourier cross-correlation analysis between the continuum region of 4C +72.26 and the NGC1741 template are shown on respective rows, and the locations of the emission lines from our Subaru spectrum of Fig. 8 are also shown, compared with the CO$(4-3)$ redshift from Papadopoulos et al., 2000. The error bars correspond to the 1σ uncertainties based on our data.

The more blueshifted of the Lyman- components ($z = 3.5334$) has a redshift consistent with that measured from the narrow Hα and [O III] lines, and also the C IV and He II emission, and the richness of this emission-line spectrum indicates that it is associated with the AGN activity. The less strongly blueshifted (and narrower) Lyα emission-line system ($z = 3.5363$) is not associated with any other emission lines and we infer that this is an outflow being driven at a line-of-sight velocity of $\sim 250\,\mathrm{km\,s^{-1}}$ by the starburst in the radio galaxy host. The lower-redshift (foreground) starbust ($z = 3.5203$) has no detectable line emission associated with it, although we note that around 25% of starbursting galaxies are not associated with an extended Lyα halo (Pettini et al. 1997), so this is not especially surprising.

It is clear that the supermassive black hole and most vigorous star-forming region both lie at $z = 3.540 \pm 0.003$, while the CO(4-3) emission has a redshift $z = 3.532 \pm 0.006$ (Papodopoulos et al. 2000), which is formally consistent with the higher redshift starburst. However, it is reasonably common for the molecular gas to end up between two galaxies undergoing collisons (e.g. Zhu et al., 2007, and also Ivison et al., 2008), which may explain the slight discrepency.

The commonly-proposed scenario of radio jet-induced star formation, which has been proposed for rapidly star-forming radio galaxies, does not appear to be appropriate for 4C +72.26. We note the lack of similarity between this source and 4C 41.17, which has been proposed as a jet-induced starburst (Dey et al. 1997; Bicknell et al. 2000); that source displays extended ultraviolet emission with morphological similarities to the radio structure, whereas 4C +72.26 has a very compact UV continuum; and the velocity field of 4C 41.17 is disturbed whereas that of 4C +72.26 is smooth. In addition, the analysis in Section 3.2 has clearly demonstrated the presence of two star-forming systems aligned closely to the line of sight, yet the radio jet is not pointing along this axis; the geometry

therefore does not favour the foreground system being influenced by the radio jet and there is no need to demand that the background system is affected in this way.

Nevertheless, we consider the jet-induced starburst scenario in the manner of Bicknell et al. (2000). We first constrain the velocity of the shock from the FWHM of the emission lines in the high-excitation ($z = 3.534$) spectrum (400–500 km s^{-1}) and their blueshift with respect to the assumed systemic velocity (460 km s^{-1}). This argues for a much lower velocity shock than in 4C 41.17, and is supported by the lack of C IV emission at the nucleus, since such shocks produce very little emission from the precursor (Allen et al. 2008), and almost all the C IV flux comes from the post-shock region where it can be absorbed by the starburst-driven outflow. A shock velocity of ~ 300 km s^{-1} produces roughly equal fluxes of C IV and He II, as observed in the halo, and C IV/C III]$\sim$3.5, consistent with the weakness of the C III]$_{1909}$ line (although this lies in a region strongly affected by night sky lines and therefore we cannot measure a reliable flux for it). With the caveat about the night sky lines, we can assume with confidence that C IV/C III]$>$2.0, and compare these values with the results of Bryant et al. (2009 – their figure 13). These emission line ratios may readily be explained by photoionisation according to their simple model, and this conclusion is not altered by assuming even considerably weaker C III] emission than our deliberately conservative upper limit.

The absence of vigorous star formation in the halo region could be explained by a much lower gas density, since the timescale for gravitational instability increases with decreasing density (equation 9 of Bicknell et al. 2000; after Elmegreen & Elmegreen 1978), and there may have been insufficient time for them to collapse since the passage of the radio jet.

Using the results of Allen et al. (2008) and the scaling of Dopita & Sutherland (1996), we infer that the total Hβ luminosity of a shock with velocity $300v_{300}$ km s^{-1} propagating through a medium of density n cm^{-3} is $L_{\mathrm{H}\beta} \approx 1.7 \times 10^{32} v_{300}^{2.41} n$ W kpc^{-2}. For the specific case of a 300 km s^{-1} shock, this produces a He II luminosity $L_{\mathrm{HeII}} = 2.0 \times 10^{32} n$ W kpc^{-2}.

Integrating the He II flux over a 1.6×1.6 arcsec^2 (11.3×11.3 kpc^2) region of the halo produces a value of $f_{\mathrm{HeII}} = 8.0 \times 10^{-20}$ W m^{-2}. We note that we are likely to have missed some flux but do not apply any correction to account for this. The luminosity of this line is 1×10^{36} W, which requires $nA_{\mathrm{sh}} \approx 5000$, where A_{sh} is the area of the shock in kpc^2. Since $n \lesssim 1$ is needed to prevent star-formation on short time-scales, this result is inconsistent with the area over which we have measured the line flux.

Similarly, we can consider the situation in 4C +72.26's compact core, where the bulk of the star formation occurs. Here, the observed He II luminosity is 5×10^{35} W, although it is certain that significant emission has been lost due to the poor positioning of the IFU. Since the core is < 500 pc in size, we require a pre-shock density $n > 10^4$ cm^{-3}. This would result in a recombination density $> 10^6$ cm^{-3} and hence significant suppression of the [O III] doublet through collisional de-excitation, for which we see no evidence. In truth, the core density would need to be much higher, since the unresolved core must also include the transition region where the density drops from the high core value to the much lower value in the halo which prevents the collapse of clouds (and hence star formation) in the halo region, and the density is unlikely to vary discontinuously. Further analysis would require assumptions about a density profile in the neighbourhood of the core, which is beyond the scope of this paper.

Considering these facts, we therefore conclude that jet-induced star formation does not provide a realistic explanation for 4C +72.26. Instead, the kinematics of the two galaxies suggests that there has been a collision, such as that proposed for the $z \sim 1$ source 3C 356 (Simpson & Rawlings 2002), that has triggered the AGN activity and the star formation.

We finally note that, despite the extreme starburst we are witnessing in 4C +72.26, the rest-frame UV/optical/near-IR spectral energy distribution requires a massive stellar population with an age of a few hundred Myr to already be in place. The massive starbursts found in high-redshift radio galaxies might therefore not be directly related to the major assembly of their stellar mass, but instead due to the presence of a large gas reservoir, absent in lower-redshift systems, within which star formation is induced by a mutual trigger, although jet-induced effects may be important in individual cases such as 4C 41.17 (Bicknell et al., 2000).

6 CONCLUSIONS

We have analysed new spectroscopy of the $z \approx 3.5$ 'broad absorption-line radio galaxy' 4C +72.26, and found it to be associated with a system of two vigorously star-forming galaxies, separated from one another by 1300 ± 200 km s^{-1}, and the more active of which hosts the supermassive black hole responsible for the extended radio source. Both galaxies display P Cygni-like absorption line profiles, while the AGN host also shows Lyα emission indicative of a galaxy-wide 'superwind' (e.g., Steidel et al. 2000; Taniguchi & Shioya 2001; Matsuda et al. 2004; Smith & Jarvis 2007, Smith et al., 2008). The AGN host is also the source of a luminous, highly-ionized outflow.

We have found tentative evidence for a 40-kpc dust disc, whose size and mass are consistent with being the site of the CO emission observed by Papadopoulos et al. (2000). From several lines of argument, we have ruled out a jet-induced star-formation scenario for 4C +72.26, and instead proposed that the star formation is caused by a collision between the two galaxies. The need for an old stellar population suggests that even at $z = 3.5$ we are not witnessing the initial episode of star formation in massive elliptical galaxies.

ACKNOWLEDGMENTS

The authors would like to thank Loretta Dunne for valuable discussions. AMS acknowledges a Royal Astronomical Society Sir Norman Lockyer Fellowship. This publication was based, in part, on observations obtained at the Gemini Observatory, which is operated by the Association of Universities for Research in Astronomy, Inc., under a cooperative agreement with the NSF on behalf of the Gemini partnership: the National Science Foundation (United States), the Science and Technology Facilities Council (United Kingdom), the National Research Council (Canada), CONICYT (Chile), the Australian Research Council (Australia), Ministrio da Cincia e Tecnologia (Brazil) and Ministerio de Ciencia, Tecnologa e Innovacin Productiva (Argentina). It is also based on data collected at the Subaru Telescope, which is operated by the National Astronomical Observatory of Japan.

REFERENCES

Allen M.G., Groves B.A., Dopita M.A., Sutherland R.S., Kewley L.J., 2008, ApJS, 178, 20

Archibald E.N., Dunlop J.S., Hughes D.H., Rawlings S., Eales S.A., Ivison R.J., 2001, MNRAS, 323, 417
Archibald E.N., Dunlop J.S., Jiminez R., Friaça A.C.S., McLure R.J., Hughes D.H., 2002, MNRAS, 336, 353
Best P.N., Kaiser C.R., Heckman T.M., Kauffmann G., 2006, MNRAS, 368, L67
Bicknell G.V., Sutherland R.S., van Breugel W.J.M., Dopita M.A., Dey A., Miley G.K., 2000, ApJ, 540, 678
Bohlin R.C., Savage B.D., Drake J.F., 1978, ApJ, 224, 132
Bruzual G., Charlot S., 2003, MNRAS, 344, 1000
Bryant J.J., Johnston H. M., Broderick J. W., Hunstead R.W., De Breuck C., Gaensler B. M., 2009, MNRAS, 395, 1099
Chabrier G., 2003, PASP, 115, 763
Chambers K.C., Miley G.K., van Breugel W.J.M., 1987, Nature, 329, 604
Conti P.S., Leitherer C., Vacca W.D., 1996, ApJ, 461, L87
De Breuck C., et al., 2001, AJ, 121, 1241
Dey A., 1999, in The Most Distant Radio Galaxies, ed. H. Röttgering, P. Best, & M. Lehnert (Amsterdam: R. Netherlands Acad. Sci.), 19
Dey A., van Breugel W., Vacca W.D., Antonucci R., 1997, ApJ, 490, 698
Dopita M.A., Sutherland R.S., 1996, ApJS, 102, 161
Dunkley J., et al, 2009, ApJS, 180, 306
Elmegreen B.G., Elmegreen D.M., 1979, ApJ, 220, 1051
Elvis M., et al., 1994, ApJS, 95, 1
Fanaroff B.L., Riley J.M., 1974, MNRAS, 167, 31P
Greve T.R., Ivison R.J., Stevens J.A., 2006, Astron. Nachr., 327, 208
Hawarden T.G., Leggett S.K., Letawsky M.B., Ballantyne D.R., Casali M.M., 2001, MNRAS, 325, 563
Ivison R.J., et al., MNRAS, 380, 199
Ivison R.J., et al., 2008, MNRAS, 390, 1117
Jackson N., Eracleous M., 1995, MNRAS, 276, 1409
Jarvis M. J., Rawlings S., Eales S. A., Blundell K. M., Bunker A. J., Croft S., McLure R. J., Willott C. J., 2001, MNRAS, 326, 1585
Jarvis M.J. & McLure R.J., 2006, MNRAS, 369, 182
Leitherer C., Robert C., Heckman T., 1995, ApJS, 99, 173
Lilly S.J., Longair M.S., 1982, MNRAS, 199, 1053
Madau P., Pozzetti L., Dickinson M., 1998, ApJ, 498, 106
Martínez-Sansigre A., Rawlings S.G., Lacy M., Fadda D., Marleau F.R., Simpson C., Willott C.J. & Jarvis M.J., 2005, Nature, 436, 4
Matsuda Y. et al., 2004, AJ, 128, 569
McCarthy P.J., van Breugel W.J.M., Spinrad H., Djorgovski S., 1987, ApJ, 321, L29
McCarthy P.J., van Breugel W.J.M., Kapahi V.K., 1991, ApJ, 371, 478
McLure R.J., Jarvis M.J., 2002, MNRAS, 337, 109
McLure R.J., Jarvis M.J., 2004, MNRAS, 353, 45
McLure R.J., Jarvis M.J., Targett T.A., Dunlop J.S., Best P.N., 2006, MNRAS, 368, 1395
Miller P., Rawlings S., Saunders R., Eales S., 1992, MNRAS, 254, 93
Motohara et al., 2002, PASJ, 54, 315
Nesvadba N.P.H., Lehnert M.D., Eisenhauer F., Gilbert A., Tecza M., & Abuter R., 2006, ApJ, 650, 693
Nesvadba, N. P. H.; Lehnert, M. D.; De Breuck, C.; Gilbert, A.; van Breugel, W., 2007, A&A, 475, 145
Papadopoulos P.P., Röttgering H.J.A., van der Werf P.P., Guilloteau S., Omont A., van Breugel W.J.M., Tilanus R.P.I., 2000, ApJ, 528, 626
Pei Y.C., 1992, ApJ, 395, 130
Pentericci L., van Reveen W., Carilli C.L., Röttgering H.J.A., Miley G.K., 2000, A&AS, 145, 121
Pettini M., Steidel C.C., Dickinson M., Kellogg M., Giavalisco M., Adelberger K.L., 1997, AIPC, 408, 279
Rawlings S.G. & Jarvis M.J., 2004, MNRAS, 355, 9
Rawlings S., Willott, C.J., Hill G.J., Archibald E.N., Dunlop, J.S. & Hughes D.H., 2004, MNRAS, 351, 676
Rees M.J., 1989, MNRAS, 239, 1P
Reuland M., van Breugel W., Röttgering H.J.A., de Vries W., de Breuck C.,Stern D., 2003, ApJ, 582, 71
Reuland M., Röttgering H.J.A., van Breugel W., de Breuck C., 2004, MNRAS, 353, 377
Rocca-Volmerange B., Le Borgne D., De Breuck C., Fioc M., Moy E., 2004, A&A, 415, 931
Seymour N. et al., 2007, ApJS, 171, 353
Seymour N. et al., 2008, ApJ, 681, 1
Siebenmorgen R., Freudling, W., Krügel E., Haas, M., 2004, A&A, 421, 129
Simpson C., et al., 1999, ApJ, 525, 659
Simpson C., Rawlings S., 2002, MNRAS, 334, 511
Smail I., Ivison R.J., Blain A.W., ApJ, 490, 5
Smith D.J.B., Jarvis M.J., 2007, MNRAS, 378, 49
Smith D.J.B., Jarvis M.J., Lacy M., Martínez-Sansigre A., 2008, MNRAS, 389, 799
Steidel C.C., Adelberger K.L., Shapley A.E., Pettini M., Dickinson M., Giavalisco M., 2000, ApJ, 532, 170
Swinbank A.M., et al., 2003, ApJ, 598, 162
Swinbank A.M., Bower R.G., Smith G.P., Smail I., Kneib J.-P., Ellis R.S., Stark D.P., Bunker A.J., 2006, MNRAS, 368, 1631
Taniguchi Y., Shioya Y., 2000, ApJ, 532, 13
Vázquez G.A., Leitherer C., 2005, ApJ, 621, 695
Walborn N.R., Nichols-Bohlin J., Panek R.J., 1985, IUE Atlas of O-Type Spectra from 1200 to 1900 Å (NASA Ref. Pub. 1115)
Walborn N.R., Parker J.W., Nichols J.S., 1995, IUE Atlas of B-Type Spectra from 1200 to 1900 Å (NASA Ref. Pub. 1363)
Willott C. J., Rawlings S., Jarvis M. J., Blundell K. M., 2003, MNRAS, 339, 173
Zhu M., Gao Y., Seaquist E.R. & Dunne L., 2007, AJ, 134

This paper has been typeset from a TEX/ LATEX file prepared by the author.